ADVANCED FUNCTIONAL MATERIALS
www.afm-journal.de

Materials Views
www.MaterialsViews.com

Thin Films of Dendritic Anatase Titania Nanowires Enable Effective Hole-Blocking and Efficient Light-Harvesting for High-Performance Mesoscopic Perovskite Solar Cells

Wu-Qiang Wu, Fuzhi Huang, Dehong Chen, Yi-Bing Cheng,* and Rachel A. Caruso**

To achieve high-performance perovskite solar cells, especially with mesoscopic cell structure, the design of the electron transport layer (ETL) is of paramount importance. Highly branched anatase TiO_2 nanowires (ATNWs) with varied orientation are grown via a facile one-step hydrothermal process on a transparent conducting oxide substrate. These films show good coverage with optimization obtained by controlling the hydrothermal reaction time. A homogeneous methylammonium lead iodide ($CH_3NH_3PbI_3$) perovskite thin film is deposited onto these ATNW films forming a bilayer architecture comprising of a $CH_3NH_3PbI_3$ sensitized ATNW bottom layer and a $CH_3NH_3PbI_3$ capping layer. The formation, grain size, and uniformity of the perovskite crystals strongly depend on the degree of surface coverage and the thickness of the ATNW film. Solar cells constructed using the optimized ATNW thin films (220 nm in thickness) yield power conversion efficiencies up to 14.2% with a short-circuit photocurrent density of 20.32 mA cm^{-2}, an open-circuit photovoltage of 993 mV, and a fill factor of 0.70. The dendritic ETL and additional perovskite capping layer efficiently capture light and thus exhibit a superior light harvesting efficiency. The ATNW film is an effective hole-blocking layer and efficient electron transport medium for excellent charge separation and collection within the cells.

1. Introduction

During the past two decades, thin film optoelectronic and photovoltaic devices have been intensively developed, and are considered promising renewable energy utilization technologies as they are constructed from low-cost materials using simple fabrication processes.[1] Of particular note is the breakthrough and progress of the organic–inorganic hybrid perovskite solar cells (PSCs) that use $CH_3NH_3PbX_3$ (X = Cl, Br, or I) as efficient light harvesters.[2–5] Such perovskite light harvesters have several advantages, such as tunable optical properties,[6] high absorption coefficients,[7] very long charge carrier (electron–hole) diffusion lengths,[8] as well as low-temperature solution processability.[9,10] To date, the record cell efficiency has been certified at 20.1%, which was achieved with a state-of-the-art mesoscopic structured device.[11,12]

Currently, three main device architectures have been explored in PSCs: (1) mesoscopic sensitized structures employing mesoporous semiconducting metal oxides (i.e., TiO_2, ZnO, WO_3, and $SrTiO_3$)[3,13–17] as the electron transport layer (ETL), (2) planar heterojunction structures (*p-i-n* solar cells) without a mesoporous layer,[4,18,19] and (3) meso-superstructured solar cells employing insulating Al_2O_3 or ZrO_2 as a scaffold layer.[17,20] In mesoscopic PSCs, the ETL that selectively and efficiently extracts the photogenerated electrons from the perovskite light absorber is of great significance. The morphology, thickness, and crystallinity of this semiconductor layer play a crucial role in the overall power conversion efficiency (PCE) of the devices. During the past few years, research based on the dominating mesoporous TiO_2 ETL has led to PCEs exceeding 17% when the interfacial engineering of the ETL/perovskite and perovskite/hole transport layer (HTL) has been optimized.[21] However, for these conventional $CH_3NH_3PbX_3$-sensitized mesoporous TiO_2 films prepared via two step procedures including a spin-coating and a subsequent dipping treatment, poor pore-filling with the perovskite sensitizer and infiltration of the hole transport medium (HTM) often occurred due to the highly convoluted porous channels within the nanoparticulate film.[22,23] Park and coworkers reported a perovskite-adsorbed submicrometer-thick rutile TiO_2 nanorod film that yielded a PCE of 9.4%.[22] Very recently, 900 nm rutile TiO_2 nanowires with large voids have been employed for PSCs exhibiting a PCE as high as 11.7%.[23] Such nanorods or nanowires are better for sensitizer anchoring, facile infiltration of the HTM, while at the same time being superior in electron transport and suppressing electron/hole recombination than nanoparticulate films when applied in PSCs. Similarly, other 1D oxide nanowire nanostructures, for instance TiO_2 nanofibers or ZnO nanorods, were also utilized

W.-Q. Wu, Dr. D. Chen, Prof. R. A. Caruso
Particulate Fluids Processing Centre
School of Chemistry, The University of Melbourne
Parkville, Victoria 3010, Australia
E-mail: dehongc@unimelb.edu.au;
rcaruso@unimelb.edu.au
Dr. F. Huang, Prof. Y.-B. Cheng
Department of Materials Science
and Engineering
Monash University
Victoria 3800, Australia
E-mail: yibing.cheng@monash.edu
Prof. R. A. Caruso
CSIRO Manufacturing Flagship
Private Bag 10, Clayton South, Victoria 3169, Australia

DOI: 10.1002/adfm.201500616

as efficient ETLs in PSCs.[13,24] However, the photovoltaic performance and interfacial electronic behavior of these PSCs based on 1D nanostructured ETLs with surface-decorated $CH_3NH_3PbX_3$ nanocrystals are strongly dependent on the length of the oxide arrays. Normally a length over 500 nm is a prerequisite for ensuring sufficient sensitizer loading and thus light absorption. Anatase TiO_2 has better structural and transport properties than rutile TiO_2, and thus achieves better photovoltaic performance in dye-sensitized solar cells.[25] Still, it remains a challenge to prepare anatase TiO_2 nanowire (ATNW) thin films with good hole blocking properties for efficient PSCs.

Herein, high quality dendritic anatase TiO_2 nanowire thin films (80–220 nm in thickness) consisting of oblique, dense, and cross-linked nanostructures have been grown directly on a transparent conducting oxide (TCO) film via a mild one-step hydrothermal process. This technique has potential i) to achieve precise control over the nanostructure morphology, film thickness, and uniformity, ii) to give excellent electrical contact between the oxide active layer and the substrate, and iii) for mass production with high-reproducibility and low-cost. It is worth noting that no additional TiO_2 compact layer was inserted between the ATNW thin film and F-doped tin oxide (FTO) glass, which is different from previously reported mesoporous TiO_2 ETLs. This is because the dendritic ATNW thin films form a highly branched and interconnected network that can serve as an effective hole-blocking layer and also provide a porous scaffold for efficient perovskite loading. Additionally, the uniformity and grain size of the perovskite is important for improving the PCE of PSCs.[26,27] In the present work, a gas-assisted approach has been employed in the spin-coating perovskite deposition procedure, which could improve infiltration of the $CH_3NH_3PbI_3$ solution into the porous network of the ATNW thin films and accelerate the evaporation of solvent and perovskite crystallization. This leads to a bilayer structure comprising of a perovskite-sensitized ATNW bottom layer and a perovskite capping layer with uniform thickness and coverage over a large area. The benefits of these high-quality, well-covering ATNW thin films are that they simultaneously show good optical transparency and hole-blocking properties. It is also worth noting that both the light harvesting ATNW/perovskite layer and perovskite capping layer could exhibit specific charge blocking effects for reduced interfacial recombination loss and demonstrate a synergistic effect of light capturing and scattering for minimal light absorption loss. Consequently, improved photocurrent, photovoltage, and fill factor result from these ATNW thin film based PSCs.

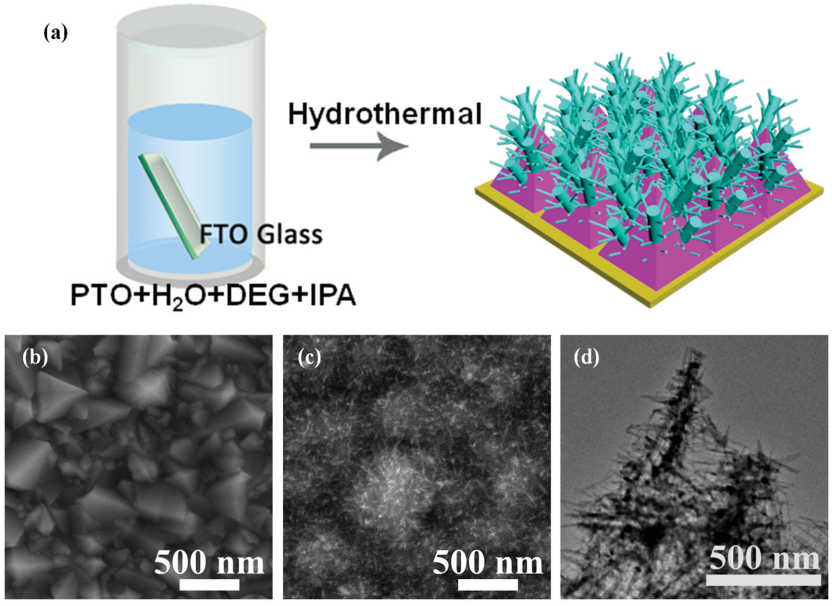

Figure 1. a) Sketch of the one-step facile hydrothermal process to fabricate TiO_2 nanowire thin films on FTO glass; SEM images of the surface morphologies of FTO glass b) before and c) after the hydrothermal treatment in PTO/H_2O/DEG/IPA solution at 190 °C for 6 h; d) TEM image of as-prepared TiO_2 nanowires scratched from the FTO glass, clearly indicating their dendritic nanostructure.

2. Results and Discussion

Hydrothermal treatment techniques are highly promising for the preparation of various TiO_2 nanomaterials with precisely controlled structural, optical, as well as electrical properties.[28–30] **Figure 1** shows schematically the hydrothermal treatment of potassium titanium oxide oxalate dehydrate (PTO) in a solution of deionized water, diethylene glycol (DEG), and isopropanol (IPA) to produce TiO_2 nanowires on FTO glass. There is a distinct difference in the top-view scanning electron microscopy (SEM) images for the pristine FTO glass (Figure 1b) and the nanowire-covered FTO glass (prepared at 190 °C with a growth period of 6 h, Figure 1c). Although the FTO crystal profile is still recognized, the surface roughness changed after the conformal hydrothermal growth of oblique and cross-linked nanowires, which shows that numerous nanowires are distributed uniformly over the FTO substrate.

The surface morphologies were further investigated by tapping-mode atomic force microscopy (AFM). Figure S1, Supporting Information, shows the topographical images of the FTO surface before and after the hydrothermal treatment. The morphology of pristine FTO became rougher after the hydrothermal treatment, and many tiny grains can be observed on the surface, which is consistent with the SEM images in Figure 1b,c. The transmission electron microscope (TEM) image (Figure 1d) of several TiO_2 nanowires cleaved from the FTO substrate shows a dendritic architecture. The branched TiO_2 nanowire is made of an elongated main trunk (≈20–30 nm in diameter) and numerous tiny branches (≈3–5 nm in diameter).

It has been widely demonstrated that rutile, anatase, or mixed crystal phase (rutile and anatase) TiO_2 nanomaterials can be obtained through hydrothermal approaches by adjusting the experimental conditions and parameters, such as Ti precursor species, solvent composition and volume ratio, and hydrothermal temperature.[31,32] The X-ray diffraction (XRD) pattern of the nanowire thin film is displayed in Figure S2a,

Supporting Information. This pattern is indexed to the three main characteristic anatase TiO_2 peaks, the (101), (200), and (105) reflections (JCPDS 21-1272), indicating the well-crystallized anatase nature of the as-synthesized TiO_2 nanowire film.

In addition, the ATNW thin film electrode exhibited similar optical transmittance compared to that of bare FTO (Figure S2b, Supporting Information). The inset in Figure S2b, Supporting Information, also indicates the high transparency of the hydrothermally processed ATNW thin film on FTO glass. Such an optical property is important for substrates in thin film optoelectronic devices, such as the perovskite solar cell. It is worth noting that the key point to fabricate nanowire thin films is the very low PTO concentration (3×10^{-3} M), which governs the film thickness of the resulting nanowires (variation in the length of the nanowires from 120 nm to 4 μm will be discussed later). Specifically, the low PTO concentration leads to unsaturated Ti (IV) species in an aqueous solution that benefits the formation of a well-covering thin film of ATNWs. A sample prepared in the absence of DEG and IPA had an inhomogeneous TiO_2 nanoparticle coverage on the FTO glass, see SEM image in Figure S3, Supporting Information. These results demonstrate that growth of the ATNWs on FTO is influenced by the presence of DEG and IPA during the hydrothermal process. DEG can restrain hydrolysis of Ti precursors,[31,33] while the IPA serves as a shape-directing agent, influencing the crystal growth of TiO_2 towards particular facets, and thus leading to the formation of TiO_2 nanowire structures with epitaxial orientation and dendritic architecture. This hydrothermal strategy provides a mild, hence green, and facile approach to fabricate TiO_2 nanowire thin films with good coverage on TCO substrates with high reproducibility.

The as-prepared ATNW thin films were loaded with perovskite sensitizer for PSC application via a gas-assisted spin-coating process that involves solution coating, gas blowing, film drying and annealing, as schematically illustrated in **Figure 2**a. First, a PbI_2/CH_3NH_3I/DMF solution was spread over the entire surface of the FTO/ATNW and the spin-coater was accelerated to the desired rotational speed of 6500 rpm for 2 s. Argon gas (60 psi) was then blown directly on the solution surface during spinning, which dried the film instantly. The advantages of applying the gas flow are that it speeds up the evaporation of the solvent and accelerates supersaturation of the solution.[19] The evaporation rate for the diethylformamide (DMF) solvent in the perovskite solution is quite slow due to its high boiling point (153 °C) and low vapor pressure (2.6 mm Hg at 20 °C). Hence the gas-assisted approach results in fast drying of the film, which induces a large number of nuclei in the solution and thereby inhibits the preferential abnormal crystal growth of perovskite.[19] Gas flow onto the surface of the solution will also benefit diffusion of the solution, and hence perovskite molecules, into the pores of the interconnected nanowire network and produce a uniform spin-coated perovskite layer. Subsequently, after 30 s rotation, an orange film was formed on top of the substrate that was converted into a highly uniform and

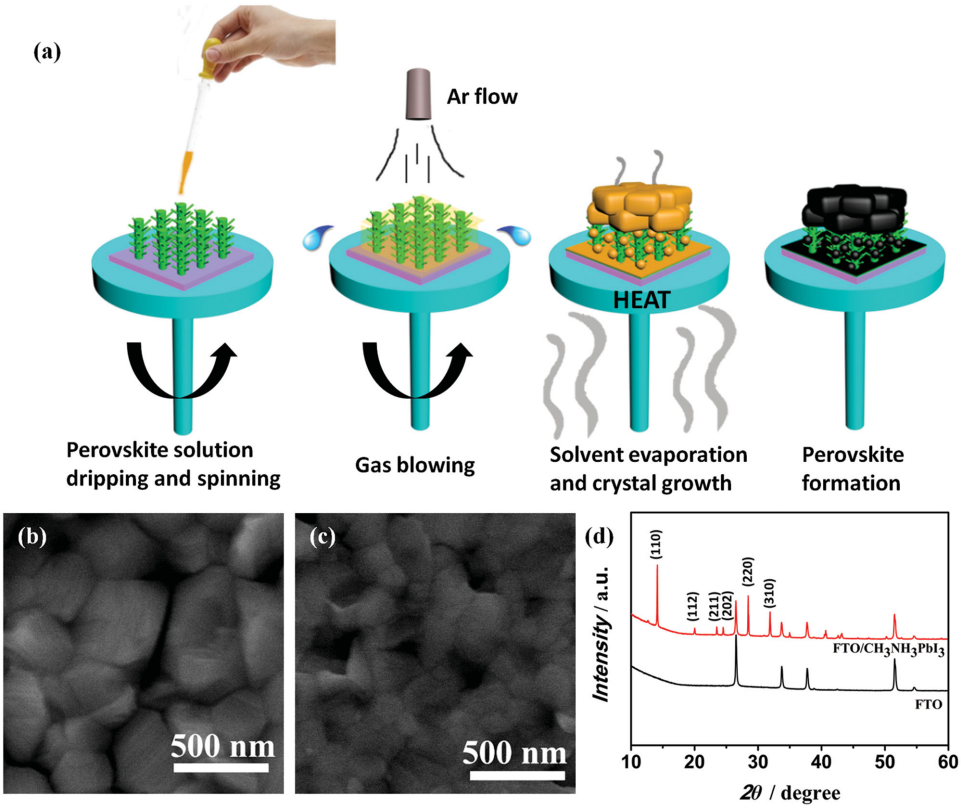

Figure 2. a) Schematic diagram of the gas-assisted evaporation and crystallization procedure for preparing a uniform perovskite film with bilayer structure. SEM images of the surface of deposited perovskite film on b) bare FTO glass and c) FTO/ATNW substrate. d) XRD patterns of the bare FTO glass substrate and perovskite film coated FTO glass substrate.

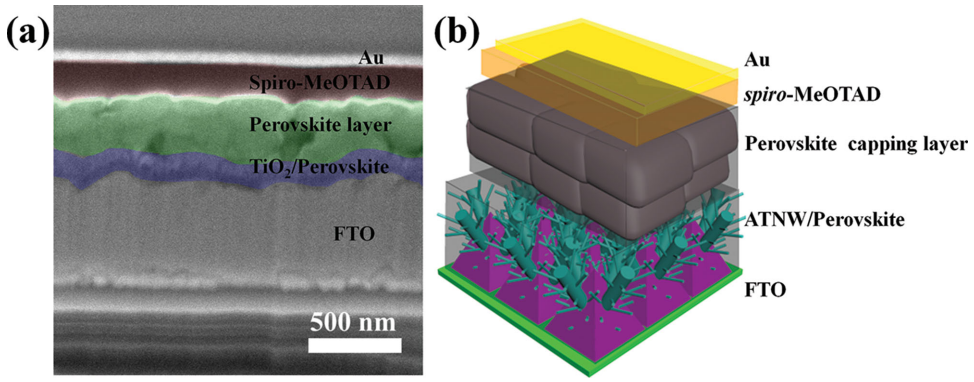

Figure 3. a) FIB-prepared cross-sectional SEM image and b) corresponding schematic architecture of perovskite solar cell constructed on the ATNW charge collection layer on FTO glass.

crystalline perovskite (dark color) when annealed on a hot plate at 100 °C for 10 min. A perovskite film deposited directly on bare FTO was also fabricated via the same gas-assisted spin-coating procedure as a control sample.

Top-view SEM images of the perovskite films on FTO and FTO/ATNW substrates are shown in Figure 2b,c, highlighting the difference in perovskite crystal size (ca. 250–500 nm on FTO glass and 80–200 nm on the FTO/ATNW substrate). The composition and crystallinity of the perovskite film on FTO glass was investigated by XRD, Figure 2d. The strong Bragg peaks at 14.08°, 28.41°, and 31.85° can be indexed to the (110), (220), and (310) diffractions of the $CH_3NH_3PbI_3$ crystal, which corresponds to the tetragonal $I4_{cm}$ crystal structure of the tri-halide perovskite with high crystallinity.[3,5] No additional PbI_2 peaks were observed in the XRD pattern, indicating a pure perovskite phase was formed under the gas-assisted film-fabrication technique. The accelerated crystal formation and growth rate are effective at optimizing the ETL/perovskite interface by yielding a uniform perovskite coverage with larger grain sizes. However, the smaller crystal size of the top perovskite layer in the case of the FTO/ATNW/perovskite substrate (mesoscopic case) with respect to the FTO/perovskite (planar case) counterpart merits attention. This difference can be ascribed to the different localized nucleation and crystal growth behavior.[21] A plausible mechanism, Figure S4, Supporting Information, shows in the planar case, the gas-assisted spin-coating leads to a fast drying process then formation of a dense film with compacted grains resulting in a monolayer of large perovskite crystals on the FTO substrate.[19] In the mesoscopic case, the seed crystals were sparsely distributed within voids between the TiO_2 nanowires. Due to the space limitations between these TiO_2 nanowires, the perovskite crystal growth was confined and a perovskite top layer consisting of multiple polycrystalline grains and relatively small crystal size was observed.

The light harvesting efficiency (LHE), which was evaluated from the absorbance properties of the electrodes, increased with perovskite film deposition on the substrate in the visible and near-infrared wavelength region (Figure S5, Supporting Information). This again confirms the efficient panchromatic light absorption capability (from near UV to near infrared regions) of the $CH_3NH_3PbI_3$ material. Under identical conditions, the perovskite on the FTO/ATNW-6h substrate shows higher LHE than perovskite on FTO in the wavelength region from 400 to 800 nm, which indicates effective and efficient light harvesting by the FTO/ATNW/$CH_3NH_3PbI_3$ thin film. The enhancement of LHE in the presence of the ATNW thin layer can be attributed to better light capturing and utilization capability of the dendritic morphology, which can harvest the sun light omnidirectionally (Figure S6, Supporting Information).[34] The best light scattering was observed for the ATNW-6h films, Figure S6a, Supporting Information. The voids existing between the adjacent grains of perovskite can also scatter the light to some extent, leading to the enhanced light scattering capability of the ATNW-6h/perovskite film as compared to ATNW-6h, which promotes the overall light harvesting efficiency.

The PSC device was completed by spiro-MeOTAD deposition as the hole transporting layer and then thermal evaporation of a Au layer as the back contact photocathode. Digital photos of the FTO/ATNW, FTO/ATNW/Perovskite and the completed device can be seen in Figure S7, Supporting Information. **Figure 3**a shows a cross-sectional SEM image of a device formed from the FTO/ATNW/Perovskite. A schematic drawing of this structure is also given (Figure 3b). Two layers containing perovskite, consisting of a TiO_2/perovskite nanocomposite and the pure perovskite capping layer are observed. Perovskite deposition in some mesoporous scaffolds via optimized film-fabrication techniques has shown the solution can fully penetrate into the pores of TiO_2 (thus forming perovskite inside the pores) and deposit a uniform capping layer with 100% surface coverage on top of the mesoporous TiO_2 film.[12,35] Two different perovskite grain sizes can be observed here. One is the small perovskite grain in the ATNW that is limited in size due to the void space, the other is the large crystal grown on top of the ATNW films. A similar bilayer structure was observed on a film of mesoporous TiO_2 nanoparticles (≈30 nm in diameter, Figure S8, Supporting Information). It is believed that a bilayer structure combining both mesoscopic (such as the ATNW/perovskite) and planar (perovskite capping layer) structure is effective for absorbing light and collecting charges within the PSC devices.[5,12,35] The optimized device had a 220 nm ATNW layer loaded with small perovskite crystals, an additional 300 nm perovskite capping layer, a 180 nm spiro-MeOTAD layer and a 80 nm thermally evaporated Au layer as the back contact.

In conventional metal oxide based PSCs, a compact blocking layer is generally deposited on the TCO substrate first, regardless of whether a planar or mesoscopic structured device is

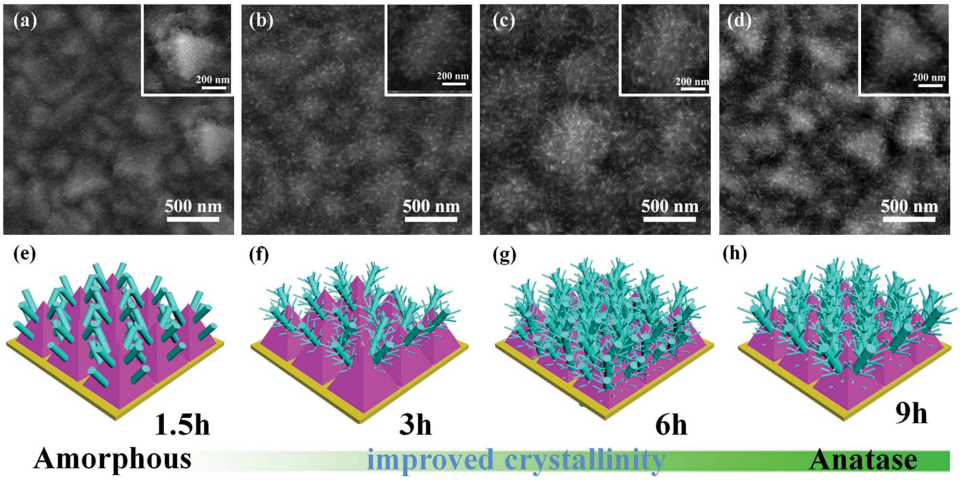

Figure 4. Top-view SEM images and corresponding sketch of TNW thin films on FTO glass hydrothermally treated at 190 °C for a,e) 1.5 h; b,f) 3 h; c,g) 6 h; and d,h) 9 h.

being fabricated.[17,20,36,37] In this study, the dense TiO_2 film made of dendritic anatase nanowires plays a significant role in preventing direct contact between FTO and perovskite, which dramatically decreases the chance of charge carrier recombination.

The morphology of the ATNW thin films evolve from the sparse nanorods to dense nanotrees by varying the hydrothermal treatment duration. **Figure 4**a–d shows the top-view SEM images of the ATNW thin films on FTO glass prepared at 190 °C for 1.5, 3, 6, and 9 h. This growth process is presented in the sketches in Figure 4e–h. In brief, sparse germination of oriented nanorods occurred at relatively short reaction time (ATNW-1.5h, Figure 4a,e). At this initial stage, one can still observe the surface of pristine FTO. Extending the hydrothermal treatment time to 3–6 h reduced the degree of order and alignment, but increased the degree of surface coverage of the dendritic nanowires, as can be seen in Figure 4b,f for ATNW-3h and Figure 4c,g for ATNW-6h. The ATNW-6h sample exhibited the most homogeneous coverage of the FTO surface, which can be ascribed to the dendritic morphology consisting of slender nanowire trunks as well as numerous branches (seen in TEM analysis, e.g., Figure 1d). However, for the ATNW-9h sample (Figure 4d,h), wider wires and a slightly lower branch density was observed compared to ATNW-6h.

Figure S9, Supporting Information, shows the XRD patterns of the different ATNW thin films. As expected, the crystal phase of the as-prepared TiO_2 film developed from amorphous (1.5 h) to pure anatase (3–9 h). The characteristic (101) and (200) peaks, which can be indexed to the anatase TiO_2 phase, became sharper with the prolonged hydrothermal duration, indicating increased crystallinity of the samples. In short, the intriguing growth of the ATNW thin films initiates with the dissolution and hydrolysis of the Ti precursor in the presence of DEG and IPA, which generates many nuclei on the surface of FTO, forming some thorn-like amorphous particles. With further reaction time (3–6 h), the particles are crystallized and grow into slender wires, while at the same time inducing growth of branches. When the reaction was carried out for 9 h, continuous growth of well-crystallized nanowires occurred at the expense of less stable nanowires, increasing the nanowire and branch diameters, and decreasing the uniformity of the coverage.[38]

The perovskite capping layer plays a crucial role as a second protection layer, preventing direct contact between the FTO and spiro-MeOTAD hole transporting material. Here, the thickness of the ATNW film can be changed by varying the reaction time or PTO concentration (discussed later) and this influences the crystal growth of the perovskite film. **Figure 5**a–d shows top-view SEM images of the perovskite capping layer on the different ATNW films. Figure S10a–d, Supporting Information, shows cross-sectional SEM images of the perovskite films deposited on ATNW films prepared with different hydrothermal treatment times (1.5–9 h). The thickness of the ATNW film and perovskite capping layer, and the grain size distribution of the perovskite crystals in the capping layer are summarized in Table S1, Supporting Information. According to cross-sectional SEM images (Figure S10a–d, Supporting Information), the density of the perovskite-coated ATNW layer indicates good filling of $CH_3NH_3PbI_3$ within the pores or wire-to-wire voids of the ATNW networks. From the top-view SEM images (Figure 5a–d), no nanowires can be observed, indicating sufficient surface coverage by the perovskite capping layer. Interestingly, the size of the $CH_3NH_3PbI_3$ grains decreases and the size distribution narrows with increasing ATNW film thickness. The crystal size of the perovskite capping layer was ≈200–450 nm for the 80 nm-thick ATNW layer (1.5 h), ≈150–380 nm for the 120 nm-thick ATNW layer (3 h), ≈150–300 nm for the 180 nm-thick ATNW layer (9 h) and ≈80–200 nm for the 220 nm-thick ATNW layer (6 h). An explanation for this pattern in crystal growth is that as the ATNW increases in thickness, the perovskite nuclei density increases (with more porous network structure to infiltrate), therefore resulting in smaller crystal size.[39] The thickness of the capping layer does not vary substantially between the films and the perovskite grains are well-defined across the film thickness. From another perspective, it can be concluded that the construction and formation rate of the perovskite film is faster in thicker ATNW films. While for the capping layer consisting of large grains, more

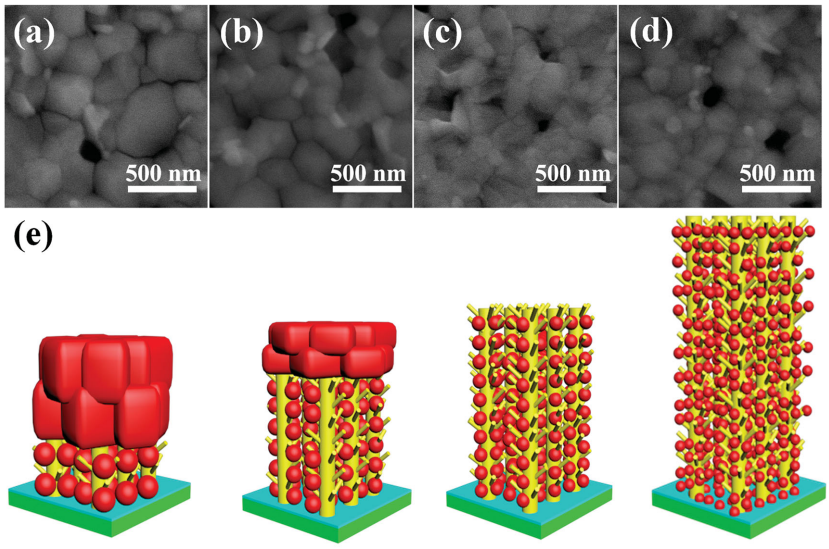

Figure 5. Top-view SEM images of the perovskite capping layer deposited on these different TNW thin films: a) 1.5 h; b) 3 h; c) 6 h; and d) 9 h. e) Sketch showing the dependence of the perovskite crystal size as well as capping layer thickness on the TNW film thickness (≈120 nm to 4 µm).

time is required for the grain coarsening process, with growth of larger grains at the expense of small grains.[26] In addition, the XRD patterns of different FTO/ATNW/perovskite electrodes were obtained to observe the influence of ATNW on the growth of the perovskite layer. However, the XRD peak intensity and the crystal orientation were very similar for all films (see Figure S11, Supporting Information).

Thicker ATNW films were constructed to further investigate the perovskite capping layer. The ATNW thickness can also be varied with changes in PTO concentration for a fixed hydrothermal temperature and duration (190 °C for 3 h). Figure S12a–i, Supporting Information, shows that the average length of the ATNW increases from 120 nm to 1.6 µm, 3.3 µm, and 4.2 µm as the PTO concentration increases from 3 to 7, 10, and 15 × 10^{-3} M, respectively. The perovskite film was spin-coated onto these four ATNW films following the gas-assisted procedure used previously. Again, the perovskite crystal size decreased with an increase in the ATNW film thickness (Figure S12j–m, Supporting Information). More interestingly, the perovskite capping layer is present for 120 nm ATNW (full surface coverage consisting of densely packed grains) and absent for the 4.2 µm ATNW (perovskite crystals decorate the nanowire surface). More voids were observed from the top when the film thickness was 1.6 µm, and bare TiO_2 surface was observed when the perovskite was deposited on the thickest films, as film coverage was not complete. Hence, for increasing film thickness the perovskite crystal size decreased and the capping layer no longer existed. With increasing film thickness the film changed from a bilayer mesoscopic plus planar structure (thin film case) to a pure mesoscopic structure (thick film case), shown schematically in Figure 5e. The ATNW and perovskite infiltrated films can be seen in the photos in Figure S12n,o, Supporting Information.

The ATNW thin films grown on FTO glass with uniform perovskite grain structure as well as the denser surface coverage produced FTO/ATNW/$CH_3NH_3PbI_3$ thin film electrodes that are highly suitable for mesoscopic perovskite solar cells. Photovoltaic devices were fabricated to evaluate the influence of the ATNW thickness (and associated variation in the perovskite crystal) on device performance. **Figure 6**a shows *J–V* curves of the PSCs fabricated using different ATNW films under the standard AM 1.5 G illumination condition. **Table 1** summarizes the extracted short-circuit current density (J_{sc}), open-circuit voltage (V_{oc}), fill factor (FF), and PCE (η). Also, photovoltaic parameters of the PSCs without a TiO_2 ETL (bare FTO) or constructed with other reference TiO_2 electrodes (to be discussed later) are tabulated in Table S2, Supporting Information. The PSC constructed without a TiO_2 ETL results in very poor PCE of 2.68%. The $CH_3NH_3PbI_3$ perovskite is in direct contact with the FTO and thus yields a very low V_{oc} of 615 mV and FF of 0.37 (Table S2, Supporting Information). Notably, all the devices fabricated using the ATNW thin film-covered FTO substrates delivered improved PCEs (>8.22%).

The PCE increased from 8.22% to 13.97% when the hydrothermal duration to prepare the ATNW thin films increased from 1.5 to 6 h, as the J_{sc}, V_{oc}, and FF all increased. The best performing PSC device was fabricated with the ATNW-6h thin film, delivering a J_{sc} of 20.94 mA cm^{-2}, a V_{oc} of 995 mV, a FF of 0.67, and an overall PCE of 13.97%. The enhancement in J_{sc} is likely to stem from two effects resulting from the improved ATNW thin film quality. First is the improved perovskite loading for the thicker ATNW films (80 nm for the 1.5 h sample and 220 nm for the 6 h sample), therefore increasing the overall thickness of the perovskite containing layers. The presence of more light harvesters to absorb incident light would result in improved collection of incident photons and thus an increased photocurrent. From cross-sectional views of the FTO/ATNW/$CH_3NH_3PbI_3$ electrodes (Figure S10, Supporting Information), the active layer of perovskite light

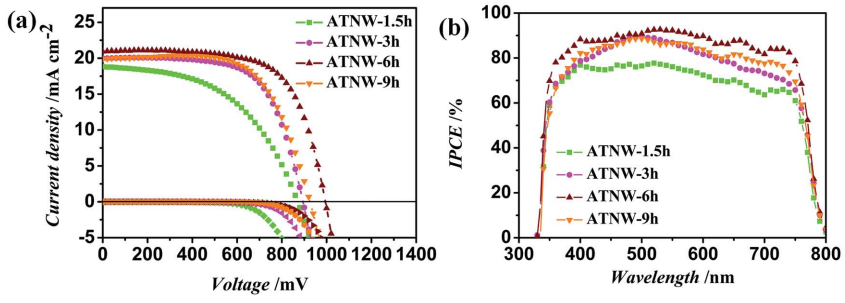

Figure 6. a) Characteristic current–voltage (*J–V*) curves and b) incident photon-to-current conversion efficiency (IPCE) spectra of the PSCs constructed using different ATNW ETLs.

Table 1. Photovoltaic parameters (J_{sc}, V_{oc}, FF, and η) of PSCs constructed using different ATNW thin film ETLs under one sun illumination (AM 1.5 G, 100 mW cm^{-2}).

Cell	J_{sc} [mA cm^{-2}]	V_{oc} [mV]	η [%]	Average η [%]	FF
ATNW-1.5h	18.83	871	8.22	7.92 ± 0.37	0.50
ATNW-3h	19.98	894	11.71	10.52 ± 0.58	0.66
ATNW-6h	20.94	995	13.97	13.25 ± 0.52	0.67
ATNW-9h	19.92	926	12.05	11.47 ± 0.46	0.65

harvester was estimated to be 430 nm for ATNW-1.5 h, 440 nm for ATNW-3 h, 520 nm for ATNW-6 h, and 490 nm for ATNW-9 h. Second, the superior light scattering capability of the dendritic ATNW layers,[34,40] as well as the densely packed perovskite capping layer, would also contribute to improved light utilization and thus affect the photocurrent. The LHE of the perovskite-deposited films containing ATNW thin films constructed with varied hydrothermal treatment durations (as indicated) was measured and is compared in Figure S5, Supporting Information. Impressively, the four films harvest the solar light from the near-UV to near infrared spectral region due to the high absorption coefficient of the $CH_3NH_3PbI_3$ light absorber.[7] The LHE increased in the order of ATNW-1.5h < ATNW-3h < ATNW-9h < ATNW-6h, and the enhanced LHE for ATNW-6h can be observed across the wavelength region from 400 to 750 nm compared to the other three samples, indicating that the ATNW based perovskite film benefits from the combined effect of a well-defined dendritic ATNW structure and sufficient perovskite film coverage. For the V_{oc} enhancement, the improved surface coverage on the FTO for ATNW-6h would inhibit direct contact of i) $CH_3NH_3PbI_3$ with the FTO, ii) spiro-MeOTAD HTM with the ETL, and iii) the back electrode with TiO_2. This would decrease the sites for recombination reactions,[15] and effectively remove shunt paths that could lead to leakage of currents.[41,42] Reducing the number of these unwanted shunt paths is expected to enhance the V_{oc}. Devices fabricated with ATNW-6h showed the highest dark current onset, Figure 6a, and its dark current increased in a slower fashion compared to devices fabricated with the other three ATNW films. This is also indicative of an effectively suppressed charge recombination for the ATNW-6h device. The higher FF of 0.67 for ATNW-6h compared with 0.50 for the ATNW-1.5h device is partly due to the improved crystallinity (from amorphous to anatase) with fewer grain boundaries and defects, and improved connection between TiO_2 and FTO after longer hydrothermal reaction time, which would decrease the series resistance and thus increase the FF.

Figure 6b shows the incident photon-to-current conversion efficiency (IPCE) spectra for the PSCs assembled using four ATNW films prepared with varied hydrothermal durations. The photocurrent generation onset is around 800 nm, which is in agreement with the observed absorption edge (corresponding to the optical bandgap, E_g = 1.55 eV) of $CH_3NH_3PbI_3$,[43] and the IPCE spectrum effectively covers the entire visible region. The ATNW film gave a noticeable IPCE enhancement over the whole wavelength region from 400–800 nm and the spectra flattened slightly as the thicker ETL film with more sufficient surface coverage was used. The relatively flat spectral profile and a high maximum IPCE over 92% are indicative of excellent light absorption and charge extraction for devices based on the ATNW-6h sample, which correlates with the best light harvesting efficiency (Figure S5, Supporting Information) and the most efficient hole-blocking capability for the ATNW-6h film. A batch of 15 cells containing ATNW-6h films has been tested, and the corresponding photovoltaic performances can be seen in Table S3, Supporting Information. The champion cell efficiency was 14.21% with a J_{sc} of 20.32 mA cm^{-2}, a V_{oc} of 993 mV, and a FF of 0.70. The results were highly reproducible, yielding an average PCE of 13.25±0.52% with a very small standard deviation in the photovoltaic performance, indicating good film and device reproducibility.

Reference cells fabricated using thin films of mesoporous TiO_2 nanoparticles (mp-TiO_2) or TiO_2 blocking layer (bl-TiO_2) with similar film thickness (≈200 nm) as the ATNW-6h were prepared for comparison. A J_{sc} of 19.40 mA cm^{-2}, V_{oc} of 934 mV, FF of 0.57, and PCE of 10.28% were obtained for the mp-TiO_2 based PSC and a J_{sc} of 17.61 mA cm^{-2}, V_{oc} of 979 mV, FF of 0.66, and PCE of 11.40% for the bl-TiO_2 based PSC, inferior results to the ATNW-6h based devices. Comparing the mp-TiO_2 and bl-TiO_2, the dense TiO_2 layer effectively inhibits charge recombination compared to the mp-TiO_2 layer, and therefore the higher V_{oc} and FF could be expected. The higher J_{sc} observed for the mp-TiO_2 device is probably due to the higher light absorption of the mesoscopic structure. Clearly the ATNW-6h based PSCs outperform devices containing these comparable films, indicating the geometry of these dense ATNW thin films (without blocking layer) is beneficial for efficient light harvesting as well as charge extraction within PSCs leading to high performance. It is also known that the electron transport is faster in dendritic TiO_2 nanowires than their nanoparticulate counterparts.[30,34] Figure S13, Supporting Information, compares the surface coverage of the mp-TiO_2 and ATNW-6 h thin films. The surface coverage is incomplete for mp-TiO_2 formed using the spin-coating process (with limited control), whereas the ATNW film achieved via the in situ hydrothermal process shows much greater coverage. Insufficient coverage would increase shunting paths with increased possibility of contact between the spiro-MeOTAD and TiO_2 layers or between the Au back electrode and TiO_2 layer. Such unwanted contact could act as a parallel diode in the solar cell equivalent circuit, causing a significant drop in V_{oc} and FF, and hence poor PCE (Figure S13c and Table S2, Supporting Information).[41] The bare FTO would allow electron/hole recombination reducing the J_{sc} and V_{oc}. This effect is not observed and hence it is believed to be effectively avoided in the ATNW thin film devices. In order to gain a better understanding of the different electron transport behavior within the branched TiO_2 nanowire (ATNW, prepared at 190 °C for 6 h) or TiO_2 nanoparticle (TNP) based electrodes, photoluminescence spectra of glass/ATNW/$CH_3NH_3PbI_3$ and glass/TNP/$CH_3NH_3PbI_3$ have been measured. As seen in Figure S14, Supporting Information, an emission peak at 780 nm can be observed for these two samples. The photoluminescence quenching in the glass/ATNW/$CH_3NH_3PbI_3$ is greater than that in glass/TNP/$CH_3NH_3PbI_3$. This indicates that the electron transport and charge extraction at the ATNW/perovskite interface is more efficient than that at

the TNP/perovskite interface, which is largely driven by the intrinsic 1D geometry of the nanowire samples.[22,23]

Hysteresis in the *J–V* curves of perovskite solar cells dependent on the direction of scan has been observed.[44–46] Thus the *J–V* curves of PSCs based on mesoscopic ATNW or planar bl-TiO_2 with different scan directions were recorded (Figure S15 and Table S4, Supporting Information). A PCE of 13.97% was recorded when using the scan direction from forward bias (FB) to short circuit (SC), while the opposite scan direction (SC–FB) yielded a PCE of 11.53%. The hysteresis could be ascribed to i) presence of the perovskite absorber in the solar cells; ii) the specific layer stacking device structures; iii) the contact interface of perovskite with n-type TiO_2 or p-type spiro-MeOTAD within the cells.[46] Smaller hysteresis and discrepancy in the *J–V* curves was observed for the mesoscopic ATNW based PSCs than the planar heterojunction bl-TiO_2 based PSCs. The ability to control the perovskite crystal growth on the ATNW and optimize the perovskite/ETL interface is being studied to decrease or even eliminate the hysteresis.

3. Conclusions

A simple, green hydrothermal technique was developed to fabricate dense thin films of anatase TiO_2 nanowires (≈220 nm) with a dendritic morphology on TCO substrates. These electron transport layers were applied in perovskite solar cells and demonstrated a PCE as high as 14.21% under AM 1.5 G illumination conditions, which is a record for NW-based solar cells to date. The gas-assisted spin-coating method for perovskite deposition gave an efficient charge collection and light harvesting electrode consisting of a perovskite-infiltrated ATNW layer and a uniform perovskite capping layer. The perovskite grain size decreased and the size distribution narrowed with increasing ATNW film thickness due to the discrepancy in nuclei density and uniformity. The multifunctionality of this dendritic ATNW thin film with dense surface coverage on the TCO substrate made it an effective ETL. The porosity of the ATNW film enabled good perovskite anchoring and TiO_2/perovskite interconnection. Moreover, the film could efficiently capture and confine the incident light, giving improved light harvesting efficiency and electron transfer from the perovskite layer and the ATNW film could serve as a good hole-blocking layer due to the varied orientation of the wires that would effectively block the direct contact between spiro-MeOTAD and FTO or between the back electrode and FTO even in the absence of a TiO_2 blocking layer. The present work shows that the hydrothermal techniques are very promising for preparing high quality and uniform metal oxide thin films on TCO substrates. The as-prepared nanowire thin films exhibited excellent optical, electrical and electrochemical properties, making them attractive for potential applications in thin film optoelectronics, including solid-state perovskite solar cells, electrochromic smart windows, and other energy storage and conversion devices.

4. Experimental Section

Fabrication of ATNW Thin Films on TCO Substrate: The TiO_2 thin films were directly grown on F-doped SnO_2 (FTO, TEC8, Dyesol) glass substrates without the assistance of a seed layer. The laser-patterned substrates were washed by sonication with soap (5% Hellmanex in water), Milli-Q water, ethanol and acetone. The solution for growing TiO_2 nanowire thin films was prepared by dissolving potassium titanium oxide oxalate dehydrate (PTO, 3×10^{-3} M, Sigma-Aldrich) in a mixed solution of Milli-Q water, diethylene glycol (DEG, Thermal Fisher), and isopropanol (IPA, Sigma-Aldrich) (volume ratio is 1:1.5:1.5, total volume is 20 mL). The cleaned substrate (2 cm × 1 cm) was immersed in the Teflon liner of an autoclave (50 mL in volume) with the FTO side facing down, and the autoclave was heated at 190 °C for 1.5–9 h. After being cooled, the nanowire thin films were rinsed with Milli-Q water and ethanol several times and then annealed at 500 °C for 1 h in air to crystallize the TiO_2 and remove any residual organic solvent. The synthesized TiO_2 nanowire thin films were soaked in 20×10^{-3} M $TiCl_4$ solution at 70 °C for 30 min and then rinsed with Milli-Q water followed by annealing at 500 °C for another 30 min.

Perovskite Film and Device Fabrication: The clear $CH_3NH_3PbI_3$ in *N,N*-diethylformamide (DMF, Sigma-Aldrich) solution (45 wt%) was prepared with PbI_2 (Sigma-Aldrich) and CH_3NH_3I (home-made) in a molar ratio of 1:1. To deposit uniform perovskite films, the gas-assisted method was employed.[19] 25 µL $CH_3NH_3PbI_3$ solution was dropped onto an ATNW coated FTO (substrate area is ≈1 cm × 1 cm). The substrate was then spun at 6500 rpm and after 2 s a dry argon gas stream (60 psi) was blown over the film to accelerate the film crystallization, and the films spun for 30 s. The color of the substrate changed from transparent to orange after 2 s. The films were then dried on a hotplate at 100 °C for 10 min. The HTM solution was prepared by dissolving 41.6 mg spiro-MeOTAD (Taiwan, Lumtec), 7.5 mL of a stock solution of 500 mg mL^{-1} lithium bis(trifluoromethylsulphonyl)imide in acetonitrile and 14.4 mL 4-tert-butylpyridine (Sigma-Aldrich) in chlorobenzene (0.5 mL). A 25 µL spiro-MeOTAD solution was coated on the perovskite film by spin-coating at 3000 rpm for 30 s. Finally, an 80 nm-thick gold layer was deposited by thermal evaporation on the spiro-MeOTAD layer as a back contact.

Characterization: The thickness and morphology of the as-prepared TiO_2 films and perovskite infiltrated films were examined by a field emission scanning electron microscope (FE-SEM, Quanta 200F FEI) and a transmission electron microscope (TEM, FEI Tecnai F20). To obtain the cross-sectional SEM image, the device was milled using a FEI Nova Dual Beam by a focused ion beam (FIB). Prior to performing the cross section, two Pt protecting layers were deposited in situ with an electron beam source at 6.3 nA and ion beam source at 0.3 nA. The milling of the cross sections used a gallium ion source at 52 ° tilting angle, 30 kV, 3 nA for regular cross-section and 0.3 nA for polishing the cross section. The AFM images were collected on a Cypher instrument (Asylum Research Company). Crystallinity and phase identification of the products was conducted using XRD (Bruker D8 Diffractometer) equipped with Cu Kα radiation (λ = 1.5418 Å). The transmittance and absorbance spectra were obtained with a UV–vis-NIR spectrometer (Lambda 1050, Perkin-Elmer) installed with a 150 mm integrating sphere. Photocurrent–photovoltage (*J–V*) characteristics of the ATNW-based perovskite solar cells were measured using a Keithley 2400 source meter under AM 1.5 G illumination (100 mW cm^{-2}) provided by an Oriel solar simulator. The incident light intensity was adjusted with a calibrated silicon photodiode (Peccell Technologies). The cells were masked with a black metal aperture of 0.16 cm^2. The IPCE spectra were recorded as a function of wavelength from 380 to 800 nm on a Keithley 2400 source meter under the irradiation of a 300 W xenon lamp fitted with an Oriel Cornerstone 260 1/4 m monochromator. The photoluminescence spectra were obtained on a FluoroMax-4 Spectrofluorometer over an emission wavelength region of 650 to 850 nm with an excitation wavelength of 460 nm.

Supporting Information

Supporting Information is available from the Wiley Online Library or from the author.

Acknowledgements

The authors acknowledge financial support from the Melbourne Research Grant Support Scheme. The Melbourne Advanced Microscopy Centre provided access to electron microscopy facilities. Support from the Australian Renewable Energy Agency and The Australian Centre for Advanced Photovoltaics is acknowledged. R.A.C. acknowledges the Australian Research Council for a Future Fellowship (FT0990583).

Received: February 12, 2015
Revised: March 26, 2015
Published online: April 17, 2015

[1] M. Grätzel, R. A. J. Janssen, D. B. Mitzi, E. H. Sargent, *Nature* **2012**, *488*, 304.
[2] A. Kojima, K. Teshima, Y. Shirai, T. Miyasaka, *J. Am. Chem. Soc.* **2009**, *131*, 6050.
[3] H. S. Kim, C. R. Lee, J. H. Im, K. B. Lee, T. Moehl, A. Marchioro, S. J. Moon, R. Humphry-Baker, J. H. Yum, J. E. Moser, M. Grätzel, N. G. Park, *Sci. Rep.* **2012**, *2*, 591.
[4] M. Z. Liu, M. B. Johnston, H. J. Snaith, *Nature* **2013**, *501*, 395.
[5] J. Burschka, N. Pellet, S. J. Moon, R. Humphry-Baker, P. Gao, M. K. Nazeeruddin, M. Grätzel, *Nature* **2013**, *499*, 316.
[6] J. H. Noh, S. H. Im, J. H. Heo, T. N. Mandal, S. I. Seok, *Nano Lett.* **2013**, *13*, 1764.
[7] G. C. Xing, N. Mathews, S. Y. Sun, S. S. Lim, Y. M. Lam, M. Grätzel, S. Mhaisalkar, T. C. Sum, *Science* **2013**, *342*, 344.
[8] S. D. Stranks, G. E. Eperon, G. Grancini, C. Menelaou, M. J. P. Alcocer, T. Leijtens, L. M. Herz, A. Petrozza, H. J. Snaith, *Science* **2013**, *342*, 341.
[9] J. T. W. Wang, J. M. Ball, E. M. Barea, A. Abate, J. A. Alexander-Webber, J. Huang, M. Saliba, I. Mora-Sero, J. Bisquert, H. J. Snaith, R. J. Nicholas, *Nano Lett.* **2014**, *14*, 724.
[10] H. P. Zhou, Q. Chen, G. Li, S. Luo, T. B. Song, H. S. Duan, Z. R. Hong, J. B. You, Y. S. Liu, Y. Yang, *Science* **2014**, *345*, 542.
[11] N. J. Jeon, J. H. Noh, Y. C. Kim, W. S. Yang, S. Ryu, S. II Seol, *Nat. Mater.* **2014**, *13*, 897.
[12] N. J. Jeon, J. H. Noh, W. S. Yang, Y. C. Kim, S. Ryu, J. Seo, S. II. Seok, *Nature* **2015**, *517*, 476.
[13] D. Y. Son, J. H. Im, H. S. Kim, N. G. Park, *J. Phys. Chem. C* **2014**, *118*, 16567.
[14] K. Mahmood, B. S. Swain, A. R. Kirmani, A. Amassian, *J. Mater. Chem. A* **2015**, DOI:10.1039/C4TA04883K.
[15] J. Zhang, P. Barboux, T. Pauporté, *Adv. Energy Mater.* **2014**, DOI:10.1002/aenm.201400932.
[16] A. Bera, K. Wu, A. Sheikh, E. Alarousu, O. F. Mohammed, T. Wu, *J. Phys. Chem. C* **2014**, *118*, 28494.
[17] A. Y. Mei, X. Li, L. F. Liu, Z. L. Ku, T. F. Liu, Y. G. Rong, M. Xu, M. Hu, J. Z. Chen, Y. Yang, M. Grätzel, H. W. Han, *Science* **2014**, *345*, 295.
[18] M. D. Xiao, F. Z. Huang, W. C. Huang, Y. Dkhissi, Y. Zhu, J. Etheridge, A. Gray-Weale, U. Bach, Y. B. Cheng, L. Spiccia, *Angew. Chem. Int. Ed.* **2014**, *53*, 9898.
[19] F. Huang, Y. Dkhissi, W. Huang, M. Xiao, I. Benesperi, S. Rubanov, Y. Zhu, X. Lin, L. Jiang, Y. Zhou, A. Gray-Weale, J. Etheridge, C. R. McNeill, R. A. Caruso, U. Bach, L. Spiccia, Y.-B. Cheng, *Nano Energy* **2014**, *10*, 10.
[20] M. M. Lee, J. Teuscher, T. Miyasaka, T. N. Murakami, H. J. Snaith, *Science* **2012**, *338*, 643.
[21] J.-H. Im, I.-H. Jang, N. Pellet, M. Grätzel, N.-G. Park, *Nat. Nanotechnol.* **2014**, *9*, 927.
[22] H. S. Kim, J. W. Lee, N. Yantara, P. P. Boix, S. A. Kulkarni, S. Mhaisalkar, M. Grätzel, N. G. Park, *Nano Lett.* **2013**, *13*, 2412.
[23] Q. Jiang, X. Sheng, Y. Li, X. Feng, T. Xu, *Chem. Commun.* **2014**, *50*, 14720.
[24] S. Dharani, H. K. Mulmudi, N. Yantara, P. T. Thu Trang, N. G. Park, M. Grätzel, S. Mhaisalkar, N. Mathews, P. P. Boix, *Nanoscale* **2014**, *6*, 1675.
[25] W. Q. Wu, H. S. Rao, Y. F. Xu, Y. F. Wang, C. Y. Su, D. B. Kuang, *Sci. Rep.* **2013**, *3*, 1892.
[26] F. Hao, C. C. Stoumpos, Z. Liu, R. P. H. Chang, M. G. Kanatzidis, *J. Am. Chem. Soc.* **2014**, *136*, 16411.
[27] Z. Xiao, Q. Dong, C. Bi, Y. Shao, Y. Yuan, J. Huang, *Adv. Mater.* **2014**, *26*, 6503.
[28] B. Liu, E. S. Aydil, *J. Am. Chem. Soc.* **2009**, *131*, 3985.
[29] X. Sheng, D. Q. He, J. Yang, K. Zhu, X. J. Feng, *Nano Lett.* **2014**, *14*, 1848.
[30] W. Q. Wu, B. X. Lei, H. S. Rao, Y. F. Xu, Y. F. Wang, C. Y. Su, D. B. Kuang, *Sci. Rep.* **2013**, *3*, 1352.
[31] W. Q. Wu, H. S. Rao, H. L. Feng, X. D. Guo, C. Y. Su, D. B. Kuang, *J. Power Sources* **2014**, *260*, 6.
[32] D. K. Roh, W. S. Chi, S. H. Ahn, H. Jeon, J. H. Kim, *ChemSuschem* **2013**, *6*, 1384.
[33] D. K. Roh, W. S. Chi, H. Jeon, S. J. Kim, J. H. Kim, *Adv. Funct. Mater.* **2014**, *24*, 379.
[34] W. Q. Wu, H. L. Feng, H. S. Rao, Y. F. Xu, D. B. Kuang, C. Y. Su, *Nat. Commun.* **2014**, *5*, 3968.
[35] J. H. Heo, S. H. Im, J. H. Noh, T. N. Mandal, C. S. Lim, J. A. Chang, Y. H. Lee, H. J. Kim, A. Sarkar, M. K. Nazeeruddin, M. Grätzel, S. I. Seok, *Nat. Photonics* **2013**, *7*, 487.
[36] D. Y. Liu, T. L. Kelly, *Nat. Photonics* **2014**, *8*, 133.
[37] O. Malinkiewicz, A. Yella, Y. H. Lee, G. M. Espallargas, M. Grätzel, M. K. Nazeeruddin, H. J. Bolink, *Nat. Photonics* **2014**, *8*, 128.
[38] W. Q. Wu, Y. F. Xu, H. S. Rao, H. L. Feng, C. Y. Su, D. B. Kuang, *Angew. Chem. Int. Ed.* **2014**, *53*, 4816.
[39] J. H. Im, I. H. Jang, N. Pellet, M. Grätzel, N. G. Park, *Nat. Nanotechnol.* **2014**, *9*, 927.
[40] W. Q. Wu, Y. F. Xu, H. S. Rao, C. Y. Su, D. B. Kuang, *J. Am. Chem. Soc.* **2014**, *136*, 6437.
[41] P. Docampo, H. J. Snaith, *Nanotechnology* **2011**, *22*, 225403.
[42] L. Y. Han, N. Koide, Y. Chiba, T. Mitate, *Appl. Phys. Lett.* **2004**, *84*, 2433.
[43] T. Baikie, Y. N. Fang, J. M. Kadro, M. Schreyer, F. X. Wei, S. G. Mhaisalkar, M. Grätzel, T. J. White, *J. Mater. Chem. A* **2013**, *1*, 5628.
[44] H. S. Kim, N. G. Park, *J. Phys. Chem. Lett.* **2014**, *5*, 3434.
[45] R. S. Sanchez, V. Gonzalez-Pedro, J. W. Lee, N. G. Park, Y. S. Kang, I. Mora-Sero, J. Bisquert, *J. Phys. Chem. Lett.* **2014**, *5*, 2357.
[46] H. J. Snaith, A. Abate, J. M. Ball, G. E. Eperon, T. Leijtens, N. K. Noel, S. D. Stranks, J. T. W. Wang, K. Wojciechowski, W. Zhang, *J. Phys. Chem. Lett.* **2014**, *5*, 1511.